Analyzing GW231109_235456 and understanding its potential implications for population studies, nuclear physics, and multi-messenger astronomy

Thibeau Wouters , Anna Puecher , Peter T. H. Pang , and Tim Dietrich , and Tim Dietrich

 Institute for Gravitational and Subatomic Physics (GRASP), Utrecht University, Princetonplein 1, 3584 CC Utrecht, The Netherlands
 Nikhef, Science Park 105, 1098 XG Amsterdam, The Netherlands

We study the gravitational-wave trigger GW231109_235456, a sub-threshold binary neutron star merger candidate observed in the first part of the fourth observing run of the LIGO-Virgo-KAGRA collaboration. Assuming the trigger is of astrophysical origin, we analyze it using state-of-the-art waveform models and investigate the robustness of the inferred source parameters under different prior choices in Bayesian inference. We assess the implications for population studies, nuclear physics, and multi-messenger astronomy. Analysing the component masses, we find that GW231109_235456 supports the proposed double Gaussian mass distribution of neutron star masses. Moreover, we find that the remnant most likely collapsed promptly to a black hole and that, because of the large distance, a possible kilonova connected to the merger was noticeably dimmer than AT2017gfo. In addition, we provide constraints on the equation of state from GW231109_235456 alone, as well as combined with GW170817 and GW190425.

In our projections for the future, we simulate a similar event using the upcoming generation of gravitational-wave detectors. Our findings indicate that we can constrain the neutron star radius with an accuracy of 400 meters using the Einstein Telescope alone, or 300 meters when combined with the Cosmic Explorer, both at 90% credibility.

I. INTRODUCTION

The first multi-messenger observation of a binary neutron star (BNS) merger, the joint observation of the gravitational wave (GW) signal GW170817 [1], the kilonova AT2017gfo [2–8], the gamma-ray burst GRB170817A [9–11] and its afterglow [12–17], showcased the importance of such observations for our understanding of cosmology and the nuclear equation of state [18, 19].

Since then, there has not been a definitive multimessenger detection of a BNS merger. However, a variety of GW and electromagnetic (EM) signals have been observed that are likely connected to BNS mergers. Among them, the GW event GW190425 [20], a compact binary merger with a total mass of $\sim 3.4 M_{\odot}$, has been identified as a BNS candidate, although the neutron star-black hole (NSBH) hypothesis cannot be ruled out [21–24]. On the EM side, GRB211211A [25–27] and GRB230307A [28] have been identified as long GRBs with strong evidence of kilonova components. However, due to the larger distance of the event and the fact that Advanced LIGO [29] and Advanced Virgo [30] were not operational at the time, it cannot be definitively confirmed that these events originated from a compact binary merger.

Recently, the fourth Gravitational-Wave Transient Catalog (GWTC-4.0) [31] reported observations from the first part of the fourth observing run (O4a) of the LIGO-Virgo-KAGRA (LVK) collaboration, but did not

include any confident BNS candidates. However, a possible sub-threshold candidate, GW231109_235456 (from here onwards, abbreviated as GW231109), has been identified as a significant trigger in a sub-threshold targeted search [32], with an inferred total mass of $2.95^{+0.38}_{-0.07}\,\rm M_{\odot}$ and a signal-to-noise ratio (SNR) of 9.7. Note that this SNR is noticeably lower than the SNR of GW170817, which was around 32.4 [33], but also below the SNR of 12.9 found for GW190425 [20]. Unfortunately, due to this low SNR, the inferred tidal deformabilities of GW231109 remain largely uninformative [32]. While a potential candidate EM counterpart was reported by Ref. [34], it is uncertain whether it originates from the same source as GW231109.

In this work, we provide a thorough analysis of the GW event to determine the properties of the source and examine its consistency with different population models. We investigate potential constraints on the equation of state (EOS) of dense nuclear matter, verifying parameter estimation consistency for different prior choices. In addition, we estimate the fate of the merger remnant, the properties of the ejecta, and predict the kilonova light curves. Finally, we simulate a system similar to GW231109 as observed by the third-generational GW detectors Einstein Telescope (ET) [35, 36] and Cosmic Explorer (CE) [37–39] to project how the increased sensitivy of these detectors would constrain the EOS from similar sources.

³ Institut für Physik und Astronomie, Universität Potsdam, Haus 28, Karl-Liebknecht-Str. 24/25, 14476, Potsdam, Germany ⁴ Max Planck Institute for Gravitational Physics (Albert Einstein Institute), Am Mühlenberg 1, Potsdam 14476, Germany (Dated: October 28, 2025)

^{*} t.r.i.wouters@uu.nl

II. GRAVITATIONAL WAVE PARAMETER ESTIMATION

Using Bayes' theorem, we sample the posterior distribution of the GW source parameters with nested sampling [40, 41]. In particular, we use the dynesty sampler [42, 43] with 2000 live points, employing the standard settings of bilby [44].

Compared to the analysis presented in Ref. [32], we introduce the following changes. First, we adopt more advanced BNS waveform models, namely, IMRPhenomXAS_NRTidalv3 for aligned spin systems and IMRPhenomXP_NRTidalv3 for systems with precessing spins [45, 46]. These models incorporate the NRTidalv3 tidal phase calibrated to unequal-mass systems with dynamical tides [45]. Second, we extend the analysis duration to 256 seconds and increase the maximum frequency to 2048 Hz to improve sensitivity to tidal effects, which are stronger at higher frequencies [47, 48]. Finally, we accelerate the likelihood evaluation using multibanding [55, 56] rather than reduced order quadrature (ROQ) [57, 58].

A. Priors

To isolate the effect of priors, we test different prior choices for the masses, spins, and tidal deformabilities of the two neutron stars (NSs). For the extrinsic parameters, the priors are identical to Ref. [59], with the luminosity distance prior uniform in comoving volume and source frame time.

Masses: We consider four mass prior choices for this analysis. First, the 'default' prior samples uniformly over detector-frame component masses while restricting the detector-frame chirp mass \mathcal{M}_c to the range $[1.29, 1.32] \,\mathrm{M}_{\odot}$, and the mass ratio $q = m_2/m_1$ to the range [0.125, 1], following standard GW inference practice.² Second, the 'uniform' prior adopts a uniform distribution over source-frame component masses in $[1,3] \,\mathrm{M}_{\odot}$, consistent with the NS population observed in GWs [60, 61]. Third, the 'Gaussian' population prior [62-64], draws sourceframe component masses from a Gaussian distribution $\mathcal{N}(1.33\,\mathrm{M}_{\odot},(0.09\,\mathrm{M}_{\odot})^2)$. Fourth, the 'double Gaussian' population prior [65–70], draws the source-frame masses from a weighted mixture³ of two Gaussian distributions, i.e., $\mathcal{N}(1.372\,\mathrm{M}_{\odot}, (0.05768\,\mathrm{M}_{\odot})^2)$ with a relative weight of 0.7137, and $\mathcal{N}(1.534\,\mathrm{M}_\odot, (0.09102\,\mathrm{M}_\odot)^2)$ with a relative weight of 0.2863, which is identical to Ref. [32].

Spins: For the magnitude of the dimensionless component spins a_i , we consider two uniform priors where the maximum magnitude is either 0.05 or 0.4, referred to as the low-spin and high-spin priors, respectively. If not specified otherwise, our fiducial runs use the low-spin prior $a_i < 0.05$. Although the maximum known spin for an NS in a binary system is ~ 0.2 [71], the limit used in the high-spin prior corresponds to the maximum spin observed in isolated NSs [71]. Note that theoretical calculations suggest that dimensionless spins can exceed this value [72].

Tidal deformabilities: The information about matter effects is primarily encoded in the dimensionless tidal deformability parameters Λ_i , which describe the deformation of an NS in a binary system as a consequence of the gravitational field created by its companion [73– 75]. We consider three priors for the tidal deformabilities in this work. First, we sample Λ_i uniformly in the range [0,5000]. Second, we use quasi-universal relations (QUR), which are relations between source parameters that are largely independent of the specific EOS. Specifically, we use the binary Love relations [76] and follow the approach outlined in Ref. [77], while acknowledging the associated caveats and drawbacks discussed in Ref. [78]. Finally, we perform parameter estimation by sampling a set of EOSs constrained by observations. In particular, we use the set of EOSs from Ref. [79] (with data available at Ref. [80]) and the weights derived by the observations collected in 'Set A'. 4 At each likelihood evaluation, the sampled EOS is used to compute Λ_i following the implementation in Ref. [81].

Our fiducial prior choice for the individual analyses discussed in the following depends on the specific question being addressed. For inferring the EOS in Sec. II D, we use posteriors obtained by sampling Λ_i uniformly in the range [0, 5000], to guarantee that the prior remains agnostic to existing EOS constraints. In contrast, for predicting the fate of the remnant (Sec. II E) and potential kilonova lightcurves (Sec. II F), we restrict ourselves to posteriors that perform EOS sampling to ensure that the masses and tidal deformabilities samples are consistent with physical constraints imposed by the EOS.

B. Source properties

Figure 1 shows the one- and two-dimensional posteriors for the source-frame component masses recovered for GW231109, compared to other low-mass GW observations that likely contained at least one NS. For GW170817, GW190425, and GW231109, the default

¹ The on-source power spectral density (PSD) is computed with BAYESWAVE [49–51] with open-data strain from GWOSC [52–54].

 $^{^2}$ The specific range for the chirp mass was chosen in order to contain the value of $1.306\,\rm M_\odot$ recovered by the template search [32].

³ See Ref. [69] for the definition of the relative weight.

⁴ 'Set A' contains information obtained from chiral effective field theory, perturbative quantum chromodynamics, radio measurements of massive pulsars, the X-ray NICER measurement of PSR J0030+0451 and PSR J0740+6620, and the analysis of GW170817; see Ref. [79] for details.

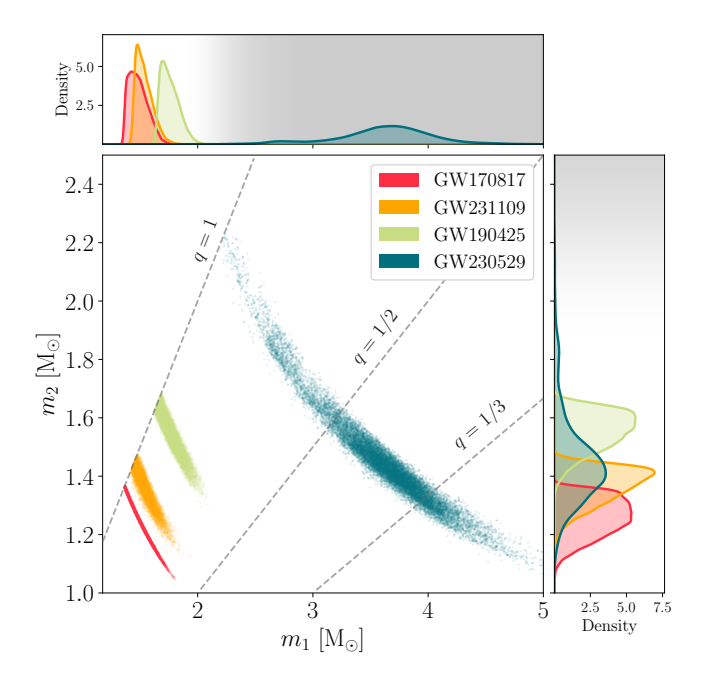


FIG. 1: Source-frame component masses of low-mass GW events that most likely contain at least one NS, namely, GW170817 [1], GW190425 [20], GW230529 [82], and GW231109_235456 (GW231109). GW231109's individual masses lie between those of GW170817 and GW190425. The gray shade in the 1D panels shows the transition from NS to BH masses: the color opacity corresponds to the cumulative density function of the TOV mass posterior, based on the uncertainty in the TOV mass inferred later in this work from measurements of heavy pulsars (see Sec. II D for details).

mass, low-spin, and uniform in Λ_i priors were used. For GW230529, we vary the magnitude of the spin of the black hole (BH) up to 0.99. The masses of GW231109 are consistent with those expected for a BNS system, being slightly heavier than those of GW170817 but still lighter than those of GW190425.

Figure 2 shows the posteriors for chirp mass \mathcal{M}_c , mass ratio q, effective spin χ_{eff} [83, 84]

$$\chi_{\text{eff}} = \frac{\chi_1 m_1 + \chi_2 m_2}{m_1 + m_2} \,, \tag{1}$$

where χ_i are the component aligned spins, and mass-weighted tidal deformability [85, 86]

$$\tilde{\Lambda} = \frac{16}{3} \frac{(m_1 + 12m_2) m_1^4 \Lambda_1 + (m_2 + 12m_1) m_2^4 \Lambda_2}{(m_1 + m_2)^5} . \quad (2)$$

The left panel of Fig. 2 shows the posterior with Λ_i sampled uniformly in [0,5000], while the right panel is obtained by sampling the EOS; cf. Sec. II A. In both cases, we show our different spin prior choices and we use the default mass priors as defined in Sec. II A. We find consistent results across the different mass prior choices.

For the posteriors obtained from sampling the EOS, we remove posterior samples for which the primary mass m_1 exceeds the Tolman-Oppenheimer-Volkoff (TOV) mass of the corresponding EOS.

We find that the broader spin priors result in wider posteriors on the masses, regardless of the prior choice on the tidal deformabilities. This is due to the correlation between mass ratio and spin [87]. When using a larger spin prior, we observe a stronger support for high positive spin values. In these cases, the inspiral process is generally decelerated due to the repulsive spin-orbit interactions that occur at the 1.5 post-Newtonian order. However, this deceleration can be offset if the system's mass ratio is lower. Therefore, systems that are both highly spinning and more asymmetric can generate similar GW signatures. Additionally, attractive tidal effects can also help counterbalance the higher spins. Indeed, the posterior using the uniform prior on tidal deformabilities recovers higher tidal deformabilities when using the high-spin prior.

When directly sampling over the EOS, we obtain slightly narrower posteriors on the masses and, consequently, on the spins. The posterior on $\tilde{\Lambda}$ coincides quite well for both spin priors when sampling the EOS, despite the large spin prior resulting in a broader posterior on the mass ratio. However, the tighter constraints on $\tilde{\Lambda}$ relative to the default prior runs stem from the information already incorporated into the EOS prior employed. Therefore, also in this case, the posterior on $\tilde{\Lambda}$ is dominated by the prior.

C. Consistency with populations

Comparing the posteriors obtained with different mass priors to the population models that determine those priors (cf. Sec. II A) can hint at the underlying BNS population. Figure 3 shows this comparison visually with the prior and posterior distributions for the source-frame component masses in dashed and solid lines, respectively. The different colors refer to the different population models that determined the priors. As a caveat, we note that the search performed in Ref. [32] assumed a double-Gaussian population model.

To quantify the degree of similarity between the various population-prior and posterior distributions, we use the Jensen-Shannon divergence (JSD) [88]. A JSD value of 0 bits indicates that the two distributions are the same, while a value of 1 bit signifies they are completely different. The JSD values are given in Table III in Appendix A.

For both the primary and secondary masses, we observe that the distribution pair with the lowest JSD, indicating the most consistent distributions, does not correspond to the scenario in which the population prior aligns with the prior used to obtain that posterior. This suggests that the event is informative and contributes measurable information beyond the prior.

For both masses, we find that all posteriors obtained

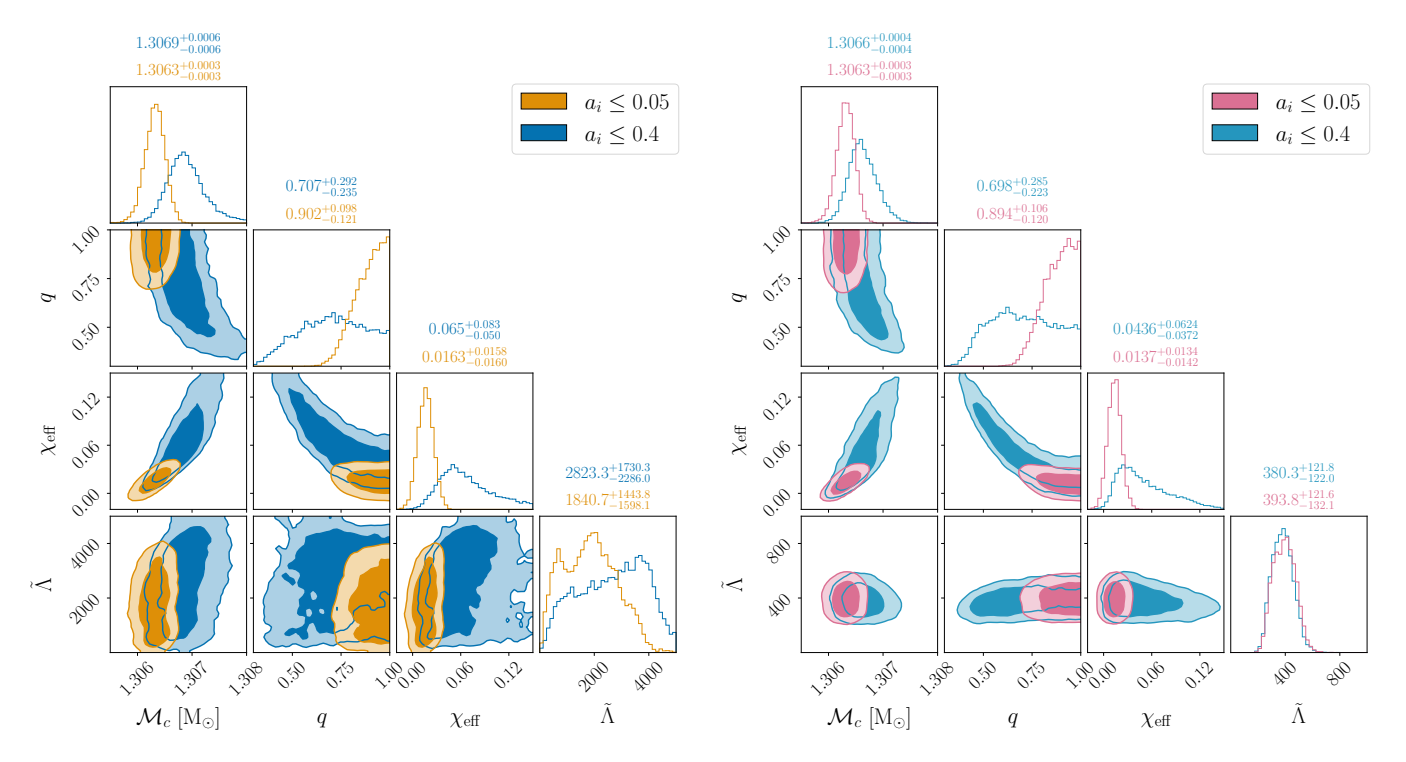


FIG. 2: Posterior on chirp mass \mathcal{M}_c , mass ratio q, effective spin $\chi_{\rm eff}$, and mass-weighted tidal deformability $\tilde{\Lambda}$ of the GW inference using the default mass priors, i.e., uniform in detector-frame component masses. Left panel: Λ_i are sampled uniformly in the range [0,5000]. Right panel: Λ_i are determined by the EOS sampled on-the-fly, with samples where the primary mass exceeds the TOV mass being discarded. The light (dark) shading indicates the 68% (95%) credible area. The median values of the recovered parameters, together with the 90% credible intervals, are reported above the marginalized posterior distributions.

with various priors are most consistent with the double Gaussian prior. This indicates that the double-Gaussian population model adequately represents both the primary and secondary mass distributions for this event.

D. Implications for the equation of state

We use the posteriors on the masses and tidal deformabilities obtained in Sec. IIB to constrain the EOS with the same setup as Ref. [89], which we briefly detail below.

Our EOS parametrization consists of three different parts. First, below a density of $0.5 n_{\rm sat}$, the EOS is fixed to the crust model from Ref. [90]. Here, $n_{\rm sat} = 0.16 \,\rm fm^{-3}$ denotes the nuclear saturation density. Second, between $0.5 n_{\rm sat}$ and a breakdown density $n_{\rm break}$, which is varied uniformly on-the-fly during sampling between [1, 2] $n_{\rm sat}$ [91], we employ the metamodel parametrization of the EOS [92–94]. Third, the high-density part of the

EOS, i.e., in the range $[n_{\text{break}}, 25 n_{\text{sat}}]$, is parametrized by grid points in the sound speed profile $c_s^2(n)$, from which the pressure-density relation can be computed [91, 95–97].

To obtain posteriors over the EOS, we use JESTER [89], which allows us to directly sample our high-dimensional (in particular, 26-dimensional) EOS parametrization by accelerating the inference with JAX [98]. In particular, the code is executed on a graphical processing unit (GPU), and we use FLOWMC, an efficient normalizing flow-enhanced Markov chain Monte Carlo (MCMC) sampler [99, 100].

During sampling, we incorporate a likelihood term that disfavors EOSs predicting a TOV mass below the mass of the heaviest observed pulsars (PSRs). In particular, we use the measurements of PSR J1614-2230 [101, 102] with a mass $M=(1.937\pm0.014)~M_{\odot}$, and PSR J0740+6620 [103] with a mass $M=(2.08\pm0.07)~M_{\odot}$ (see also Refs. [104–110]).⁶ Throughout this work, we refer to this constraint as 'heavy PSRs'.

Additionally, for the BNS events considered in this work, we use the marginalized 4-dimensional posteri-

 $^{^5}$ We note that this conclusion remains also valid when using a double Gaussian with $\mathcal{N}(1.34\,\mathrm{M}_\odot,(0.08\,\mathrm{M}_\odot)^2)$ and a relative weight of 0.65, and $N(1.80\,\mathrm{M}_\odot,(0.21\,\mathrm{M}_\odot)^2)$ with a relative weight of 0.35 as in Ref. [67].

 $^{^6}$ Uncertainties on the masses are quoted at the 68% credible level.

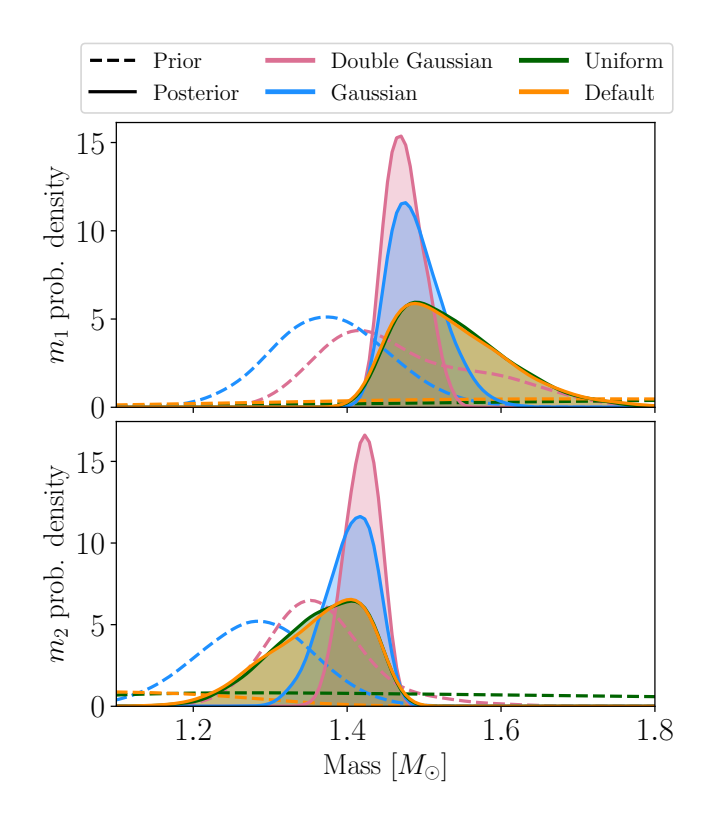


FIG. 3: Comparison between priors (dashed lines) from populations and corresponding posteriors (solid lines) of the source-frame component masses, for the four mass priors considered.

ors on the source-frame component masses and tidal deformabilities to approximate the pseudo-likelihood function for the EOS parameters. In practice, we train a normalizing flow to estimate the density of these marginal posteriors. The flows use the block neural autoregressive flow architecture [111] and are trained with FLOW-JAX [112].

Table I shows the posterior median value and 90% credible intervals of the radius of a $1.4\,\mathrm{M}_{\odot}$ NS. For GW231109, we use the posterior obtained with the default mass, low-spin, and uniform in Λ_i prior. The constraints on the TOV mass and the pressure at $3n_{\mathrm{sat}}$, as well as the results obtained from other prior choices for GW231109, are given by Table IV in Appendix B.

Both GW190425 and GW231109 align with the constraints set by heavy-pulsar measurements and do not impose any noticeable constraints, which can be attributed to their lower SNR compared to GW170817. For GW190425, moreover, the high mass of the event is expected to give poor constraints on the EOS [113]. Since both GW190425 and GW231109 prefer slightly larger $R_{1.4}$ values, the uncertainties are reduced compared to the constraints from heavy PSRs due to the support of the prior. The effect of the GW prior choices for GW231109 is minimal and well below the reported uncertainty, as shown in Table IV.

TABLE I: Posterior on $R_{1.4}$ obtained from the constraints discussed in Sec. II D, denoted by the median with 90% credible intervals as uncertainty. All inferences with GW data also include the constraints from heavy PSRs.

Dataset	$R_{1.4} [{\rm km}]$
Heavy PSRs	$13.2^{+1.0}_{-1.2}$
GW170817	$12.2^{+1.1}_{-1.4}$
GW190425	$13.5^{+0.7}_{-0.9}$
GW231109 (default)	$13.3^{+0.9}_{-1.1}$
GW170817+GW190425	$12.3^{+1.2}_{-1.2}$
GW170817+GW231109	$12.2^{+1.0}_{-1.2}$
GW170817+GW190425+GW231109	$12.1_{-1.2}^{+1.1}$

The combination of GW170817 and GW190425 yields a higher median $R_{1.4}$ value. When we combine all three BNS candidates, we find $R_{1.4} = 12.1^{+1.1}_{-1.2}$ km, compared to $12.2^{+1.1}_{-1.4}$ km when considering GW170817 alone, at 90% credibility. Overall, as expected, we find that the constraints are driven by the high-SNR signals GW170817 (as also noted by Refs. [114–116]) and that including additional low-SNR BNS candidates only leads to marginal changes.

E. Estimating the remnant fate

Depending on the properties of the system, the remnant formed during the merger process can have different lifetimes before collapsing into a BH or even remain stable [47, 117–120]. Typically, for heavier masses, the system promptly collapses to a BH. Alternatively, a differentially-rotating hyper-massive neutron star (HMNS) can be formed, with possibly higher mass than the maximum mass sustained by a uniformly rotating NS. This HMNS survives for a few milliseconds before different mechanisms dissipate the differential rotation, either causing it to collapse to a BH or, in case of slightly lower masses, to form a uniformly rotating supra-massive NS (SMNS) that survives up to $\mathcal{O}(1\,\mathrm{s})$ before collapsing. For very low-mass systems, the mass of the remnant produced by the merger can be lower than the TOV mass, and therefore a stable NS is formed.

To predict the remnant expected for this trigger, we use the classifiers developed in Ref. [121], based on gradient boost decision trees [122, 123]. In particular, three different classifiers are available: Classifier A distinguishes between prompt collapse to BH (p_{PCBH}) or formation of a NS remnant (p_{RNS}); Classifier B further distinguishes the NS remnant scenario in formation of a HMNS (p_{HMNS}) or a remnant (which could be a HMNS, SMNS, or stable NS) that survives more than 25 ms (p_{NC}); Classifier

TABLE II: Probabilities of the different merger outcomes using the three classifiers developed in Ref. [121] applied to the posteriors obtained while sampling the EOS, for both low-spin and high-spin priors.

Classifier A	$p_{\scriptscriptstyle ext{PCBH}}$	$p_{ m \scriptscriptstyle RNS}$		
Low spin	57.4%	42.6%		
High spin	79.1%	20.9%		
Classifier B	$p_{\scriptscriptstyle ext{PCBH}}$	$p_{ m HMNS}$	$p_{ m NC}$	
Low spin	57.9%	42.0%	0.1%	
High spin	79.1%	20.8%	0.1%	
Classifier C	$p_{\scriptscriptstyle ext{PCBH}}$	$p_{ m short}$	$p_{\scriptscriptstyle m LONG}$	$p_{\scriptscriptstyle ext{NC}}$
Low spin	62.8%	35.0%	2.1%	0.0%
High spin	83.1%	14.3%	1.8%	0.7%

C, in which the HMNS class is further divided into short-lived (p_{SHORT}) , i.e., for which the HMNS collapses to a BH in a time $2\,\text{ms} < \tau_{\text{BH}} < 5\,\text{ms}$, and long-lived (p_{LONG}) , i.e., with $\tau_{\text{BH}} > 5\,\text{ms}$. All three classifiers predict the remnant based on the values of source parameters that can be inferred from the inspiral signal: the total mass, the mass-weighted tidal deformability $\tilde{\Lambda}$, the mass ratio q, and the effective spin χ_{eff} .

Table II shows the probabilities for the different kinds of remnants based on the posteriors both from our fiducial run with EOS sampling and low-spin prior $(a_i <$ 0.05), and the EOS-sampling analysis with larger spin prior $(a_i < 0.4)$. We do not apply the classifier to posteriors obtained with uniform priors on the tidal deformabilities or to those assuming the QUR, since the event's low SNR leads to a poorly constrained Λ , producing samples with nonphysical combinations of masses and tidal deformabilities. In both cases and for all three classifiers, the preferred scenario is a prompt collapse to a BH, although there is a non-negligible probability for the formation of an HMNS. The prompt-collapse probability is higher for the high-spin analysis, consistent with the overall higher mass inferred (see Figure 2). In case an HMNS was formed, it was most likely short-lived, i.e., it collapsed within 5 ms from merger.

F. Estimating possible kilonova lightcurves

Given the non-negligible probability of an HMNS formation, we predict the corresponding kilonova light curves to assess what EM counterpart this event would have produced. For this purpose, we use the nuclearphysics and multi-messenger astrophysics framework NMMA [81], and employ the Bu2019lm model [124], together with the posteriors from our fiducial run with EOS sampling. The Bu2019lm model is built using POSSIS [125, 126], a radiative transfer code simulating photon packets diffusing out of the eject material. Both the dynamic ejecta mass $M_{\rm dyn}^{\rm ej}$ and the disk mass $M_{\rm disk}$ are estimated using the relations presented in Ref. [81]. The wind ejecta mass $M_{\text{wind}}^{\text{ej}}$ is assumed to be 30% of the disk mass [127, 128]. The opening angle Φ between the lanthanide-rich and lanthanidepoor dynamical ejecta components is varied within the range of [15°, 75°]. The estimated ejecta masses are $\log_{10} M_{\mathrm{dyn}}^{\mathrm{ej}}/M_{\odot} = -2.20^{+0.34}_{-0.14}$ and $\log_{10} M_{\mathrm{wind}}^{\mathrm{ej}}/M_{\odot} = -1.27^{+0.21}_{-0.02}$. The quoted values represent the median along with the 90% credible interval as uncertainty.

The estimated lightcurves, along with the observations from AT2017gfo [2–8], are presented in Figure 4. The lightcurves shown represent the median values, along with the 90% credible interval, measured in AB magnitudes across various photometric bandpasses. It is evident that for this event, at a distance of around 165 Mpc, the kilonova lightcurves are significantly dimmer than for AT2017gfo. If this event is detected by the online search pipeline, the kilonova lightcurves may be partially captured by the Zwicky Transient Facility [129, 130] and potentially fully captured by the Vera Rubin Observatory [131]. Alternatively, if the event occurred closer to us and an HMNS were formed, it would be more feasible to detect its electromagnetic signature.

Reference [34] performed a search for an EM counterpart of GW231109 with archival data and reported one candidate, AT2023xqy, to be in good agreement with the trigger time and distance reported by the GW pipelines. However, given that AT2023xqy peaks roughly 14 days after the GW trigger, our results make it challenging to interpret this transient as a plausible kilonova counterpart of GW231109.

III. INJECTIONS WITH THIRD-GENERATION DETECTORS

To evaluate the potential implications on the EOS from a source like GW231109, we simulate a similar source detected by third-generation detectors. These detectors are anticipated to observe up to $\mathcal{O}(10^4)$ BNS events annually, with around $\mathcal{O}(10^3)$ of those having an SNR greater than 100 [132, 133]. Two detector configurations are considered. First, we assume ET in its triangular xylophone configuration, with 10 km arms and located in Limburg [134]. Second, we consider ET in a network with CE, where CE is assumed to be an L-shaped detector with 40 km arm-length located at the current LIGO-Hanford site [135].

The injected parameters are the median values of the

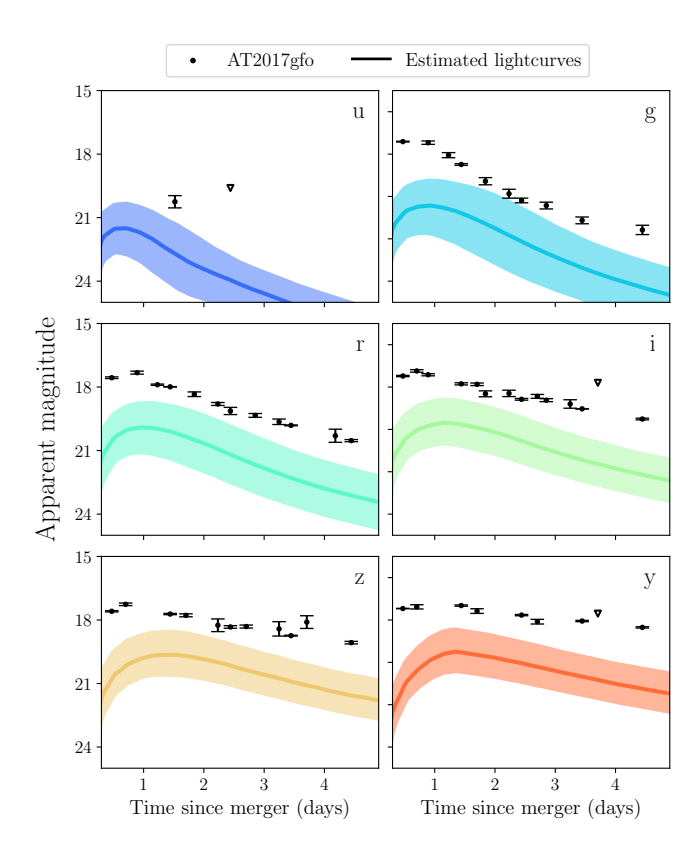


FIG. 4: The lightcurves presented with the median values, along with the 90% credible interval, measured in AB magnitudes across various photometric bandpasses. These observations are compared with data from AT2017gfo [2–8].

posteriors obtained in our fiducial analysis with EOS sampling (i.e., the low-spin prior run in the right panel of Figure 2). However, given the poor constraints on the spin angle parameters, the median values would correspond to highly precessing systems, which are not expected in the known BNS population and could induce biases in the analysis due to the models' limited calibration accuracy in this parameter region. Therefore, we simulate a system with aligned spins. The injected EOS, from which the tidal deformabilities are computed, is the maximum likelihood EOS inferred using only heavy PSRs, as described in Sec. II D. The simulated signals yield SNR values of 134 and 294 for the ET and ET+CE networks, respectively.

The recovery uses the IMRPhenomXP_NRTidalv3 waveform, without assuming aligned spins, to be consistent with the previous analyses, and with the default mass, low-spin, and uniform tidal deformability priors. The starting frequencies for the analysis are set to 5 Hz for ET and 10 Hz for CE.⁷ In this work, we do not consider

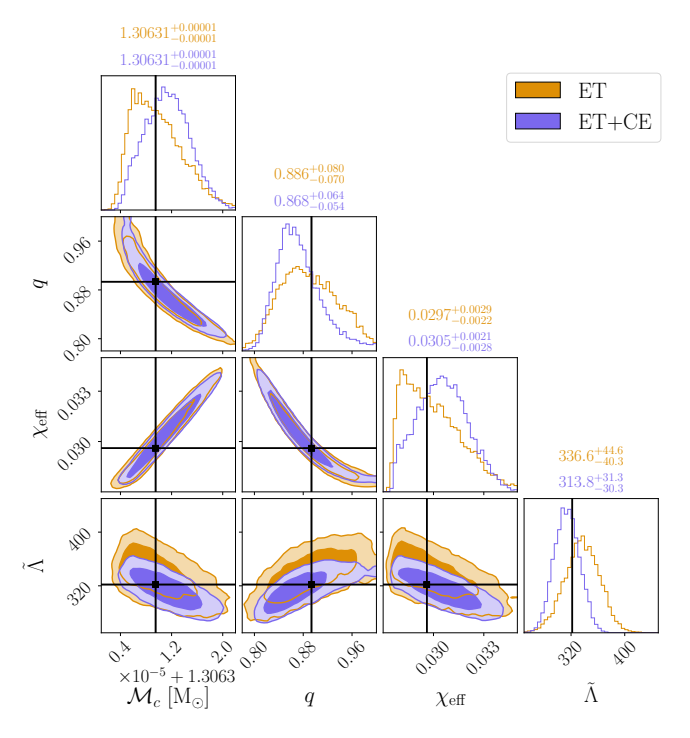


FIG. 5: Posterior on parameters from a simulated source similar to GW231109 observed with ET and a network of ET with CE. The black lines indicate the injected values. The median values of the recovered parameters, together with the 90% credible intervals, are reported above the marginalized posterior distributions.

effects from the rotation of the Earth.

Figure 5 shows the resulting posteriors for chirp mass \mathcal{M}_c , mass ratio q, effective spin $\chi_{\rm eff}$, and mass-weighted tidal deformability $\tilde{\Lambda}$. All parameters are well recovered with an improved accuracy compared to the posteriors from Figure 2, due to the higher SNR. As expected, the uncertainties are further reduced when considering ET in a network with CE.

Figure 6 shows the posteriors on the source-frame chirp mass $\mathcal{M}^{\rm src}$ and mass-weighted tidal deformabilities for the simulated source as detected by 3G detectors, compared to GW170817. The uncertainty in the sourceframe chirp mass is larger for the simulated signals compared to GW170817, despite the detector-frame chirp mass being well-measured thanks to the high SNR. This is because the redshift values in the posteriors of the simulated signals have a larger spread at the larger distance of 168 Mpc. We also show posterior samples from the EOS inference outlined in Sec. IID using GW170817 as a constraint, also shown in Table I, as well as the EOS used to compute the tidal deformabilities for the injection. The curves are plotted assuming an equal mass system for visualization. Due to the tidal deformabilities being well measured at this high SNR, the simulated events are more informative for the EOS compared to

⁷ Being planned to be built underground, ET is expected to gain sensitivity also below 10 Hz.

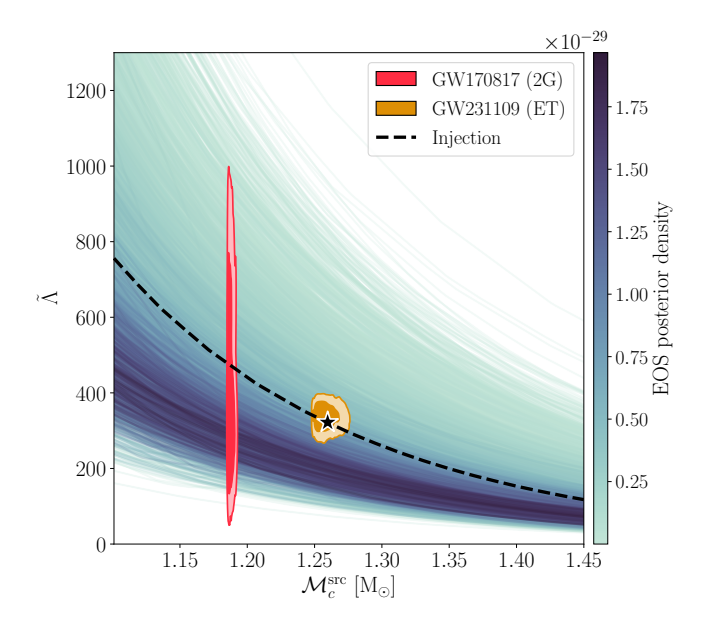


FIG. 6: Posterior samples on source-frame chirp mass and $\tilde{\Lambda}$ for GW170817 (pink) and the simulated signals (orange shades), together with posterior EOS samples constrained by GW170817, color-coded by the posterior probability. The EOS used for the injections, as well as the simulated signal, are shown in black. The light (dark) shades represent 68% (95%) credible areas.

GW170817.

Figure 7 shows the resulting constraints on $R_{1.4}$ from the posteriors shown in Figure 5, using the same setup as described in Sec. II D. The resulting constraints give $12.30^{+0.31}_{-0.36}$ km and $12.08^{+0.29}_{-0.28}$ km at the 90% credible level, for the inference using ET and ET-CE network, respectively, whereas the injected value is 12.23 km. Therefore, the uncertainties on the inferred $R_{1.4}$ are decreased significantly with third-generational GW detectors.

We note that our projection is optimistic, since, apart from precession effects, the injection and recovery use the same waveform, such that effects from waveform systematics can be ignored. This will become important for signals with an SNR above $\gtrsim 80~[136]$, when mismodelling effects in the BNS inspiral [137], or combining information from a few tens of BNS mergers [138].

IV. CONCLUSIONS

In this work, we performed investigations of GW231109_235456 (abbreviated GW231109), a subthreshold BNS candidate identified by Ref. [32] in LIGO-Virgo-KAGRA's O4a observing run. By using state-of-the-art BNS waveform models, various prior choices, and extending the frequency range of the analysis to 2048 Hz, we aim to provide a comprehensive discussion of the GW trigger and its potential implications. Due to the low SNR of the signal, prior assumptions noticeably in-

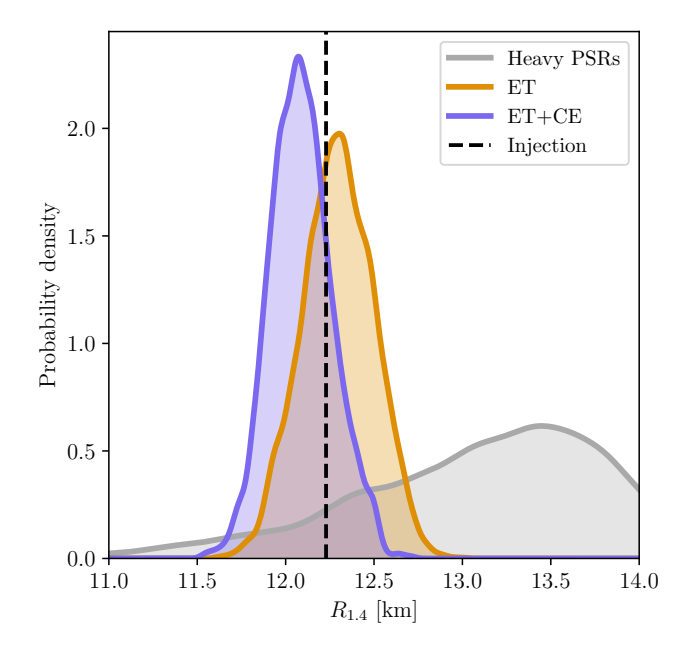


FIG. 7: Posterior constraints on $R_{1.4}$ when constrained by a GW231109-like source observed with ET, and a network consisting of ET and CE. The posterior determined by measurements of heavy pulsars is shown in gray.

fluence the final posterior distributions.

By using different priors on the source-frame component masses, we find that the source is most consistent with the double Gaussian population model.

We additionally constrain the EOS from GW231109, finding that the EOS is poorly constrained from GW231109 alone, due to the low SNR of the event. However, by combining GW231109 with GW170817 [1] and GW190425 [20], we constrain the radius of a $1.4\,\rm M_{\odot}$ NS to be $12.1^{+1.1}_{-1.2}$ km, compared to $12.2^{+1.1}_{-1.4}$ km from GW170817 alone, at the 90% credible level.

Furthermore, we predict the fate of the remnant formed after the merger using machine-learning classifiers trained on numerical-relativity simulations of BNS mergers from Ref. [121]. We find that the merger most likely led to a prompt collapse to a BH and, if an HMNS was formed first, it was likely short-lived, i.e., collapsed to a BH around 2-5 ms after merger. We also predict the lightcurves from a potential kilonova counterpart that would originate from the merger, finding that they are much dimmer than AT2017gfo [2–8] and unlikely to be detectable.

Finally, we use the inferred source properties of GW231109 to simulate a signal with similar properties as observed by ET, and a network of ET and CE. Due to the increased SNR, the source properties are better constrained, which decreases the uncertainties $R_{1.4}$ down to around 400 meters when observed with ET, and 300 meters when observed by both ET and CE.

Appendix A: Jensen-Shannon divergences

Table III shows the JSD values between the prior and posterior distributions on which the discussion presented in Sec. II C is based.

Appendix B: Constraints on EOS quantities

In Table IV we show the constraints on the EOS by summarizing a few quantities of interest. In particular, we show the TOV mass, $M_{\rm TOV}$, the radius of a $1.4\,{\rm M}_{\odot}$ NS, $R_{\rm 1.4}$, and the pressure at $3n_{\rm sat}$, $p(3n_{\rm sat})$, for the various constraints discussed in Sec. II D. The inference results using information from a BNS candidate use the same default prior as defined in Sec. II A, i.e., using the default mass prior, low-spin prior, and sampling Λ_i uniformly in the range [0,5000] for all BNS. When considering GW231109 alone, we infer the EOS by changing one aspect of these prior choices, as denoted by the brackets and explained in detail in Sec. II A. In particular, the label XAS denotes inferring the EOS from the posterior obtained when using the aligned spin waveform approximant IMRPhenomXP_NRTidalv3 in the recovery.

ACKNOWLEDGMENTS

We thank Lami Suleiman, the LIGO-Virgo-KAGRA extreme matter community, Mick Wright, and Michael Williams for fruitful discussions and feedback that led to the improvement of this work. T.W. is supported by the research program of the Netherlands Organization for Scientific Research (NWO) under grant number OCENW.XL21.XL21.038. A.P., T.D. acknowledge funding from the EU Horizon under ERC Starting Grant, no. SMArt-101076369. P.T.H.P. is supported by the research program of the Netherlands Organization for Scientific Research (NWO) under grant number VI.Veni.232.021.

We thank SURF (www.surf.nl) for the support in using the National Supercomputer Snellius under project number EINF-14622. The computations were performed on the DFG-funded research cluster Jarvis at the University of Potsdam (INST 336/173-1; project number: 502227537). Views and opinions expressed are those of the authors only and do not necessarily reflect those of the European Union or the European Research Council. Neither the European Union nor the granting authority can be held responsible for them. This research has made use of data or software obtained from the Gravitational Wave Open Science Center (gwosc.org), a service of the LIGO Scientific Collaboration, the Virgo Collaboration, and KAGRA. This material is based upon work supported by NSF's LIGO Laboratory which is a major facility fully funded by the National Science Foundation, as well as the Science and Technology Facilities Council (STFC) of the United Kingdom, the Max-Planck-Society (MPS), and the State of Niedersachsen/Germany for support of the construction of Advanced LIGO and construction and operation of the GEO600 detector. Additional support for Advanced LIGO was provided by the Australian Research Council. Virgo is funded, through the European Gravitational Observatory (EGO), by the French Centre National de Recherche Scientifique (CNRS), the Italian Istituto Nazionale di Fisica Nucleare (INFN) and the Dutch Nikhef, with contributions by institutions from Belgium, Germany, Greece, Hungary, Ireland, Japan, Monaco, Poland, Portugal, Spain. KAGRA is supported by Ministry of Education, Culture, Sports, Science and Technology (MEXT), Japan Society for the Promotion of Science (JSPS) in Japan: National Research Foundation (NRF) and Ministry of Science and ICT (MSIT) in Korea; Academia Sinica (AS) and National Science and Technology Council (NSTC) in Taiwan. T.W. acknowledges the use of generative AI (Claude Sonnet 4.5) to proofread and polish the manuscript. All AI-generated outputs were carefully reviewed and edited by T.W. to ensure accuracy.

B. P. Abbott et al. (LIGO Scientific, Virgo), Phys. Rev. Lett. 119, 161101 (2017), arXiv:1710.05832 [gr-qc].

^[2] B. P. Abbott *et al.* (LIGO Scientific, Virgo), Astrophys. J. Lett. **850**, L39 (2017), arXiv:1710.05836 [astroph.HE].

^[3] I. Andreoni *et al.*, Publ. Astron. Soc. Austral. **34**, e069 (2017), arXiv:1710.05846 [astro-ph.HE].

^[4] D. A. Coulter *et al.*, Science 358, 1556 (2017), arXiv:1710.05452 [astro-ph.HE].

^[5] V. M. Lipunov et al., Astrophys. J. Lett. 850, L1 (2017), arXiv:1710.05461 [astro-ph.HE].

^[6] B. J. Shappee et al., Science 358, 1574 (2017), arXiv:1710.05432 [astro-ph.HE].

^[7] N. R. Tanvir et al., Astrophys. J. Lett. 848, L27 (2017), arXiv:1710.05455 [astro-ph.HE].

^[8] Y. Utsumi et al. (J-GEM), Publ. Astron. Soc. Jap. 69, 101 (2017), arXiv:1710.05848 [astro-ph.HE].

^[9] B. P. Abbott et al. (LIGO Scientific, Virgo, Fermi-GBM, INTEGRAL), Astrophys. J. Lett. 848, L13 (2017), arXiv:1710.05834 [astro-ph.HE].

^[10] A. Goldstein et al., Astrophys. J. Lett. 848, L14 (2017), arXiv:1710.05446 [astro-ph.HE].

^[11] V. Savchenko et al., Astrophys. J. Lett. 848, L15 (2017), arXiv:1710.05449 [astro-ph.HE].

^[12] G. Hallinan et al., Science 358, 1579 (2017), arXiv:1710.05435 [astro-ph.HE].

^[13] K. D. Alexander et al., Astrophys. J. Lett. 863, L18 (2018), arXiv:1805.02870 [astro-ph.HE].

^[14] R. Margutti et al., Astrophys. J. Lett. 856, L18 (2018), arXiv:1801.03531 [astro-ph.HE].

	m_1 Prior			m_2 Prior					
		Default	Double Gaussian	Gaussian	Uniform	Default D	Oouble Gaussian	Gaussian	Uniform
	Default	0.68	0.20	0.56	0.76	0.81	0.04	0.22	0.58
Posterior	Double Gaussian	0.85	0.43	0.55	0.90	0.96	0.44	0.73	0.78
OST	Gaussian	0.80	0.33	0.53	0.86	0.92	0.25	0.57	0.72
	Uniform	0.68	0.21	0.57	0.77	0.82	0.04	0.23	0.59

TABLE III: JSD values (in bits) between the prior and posterior distributions of the source-frame component masses, for the various mass priors described in Sec. II A and using the default low-spin, uniform in Λ_i priors. Bold values denote the lowest JSD within each row.

TABLE IV: Constraints on M_{TOV} , $R_{1.4}$ and $p(3n_{\text{sat}})$. For GW231109, we show the constraints for various prior choices as described in Sec. II B. All constraints using BNS mergers additionally enforce the heavy pulsar constraint. All values denote 90% credible intervals.

Dataset	$M_{ m TOV} \ [M_{\odot}]$	$R_{1.4} [\mathrm{km}]$	$p(3n_{\rm sat}) \; [{\rm MeV \; fm^{-3}}]$
Heavy PSRs	$2.25^{+0.38}_{-0.31}$	$13.2^{+1.0}_{-1.2}$	98^{+62}_{-46}
GW231109 (default)	$2.29^{+0.42}_{-0.32}$	$13.3^{+0.9}_{-1.1}$	100_{-44}^{+76}
GW231109 (Gaussian)	$2.30^{+0.42}_{-0.33}$	$13.4^{+0.9}_{-1.1}$	103^{+80}_{-44}
GW231109 (double Gaussian)	$2.29_{-0.34}^{+0.39}$	$13.5^{+0.8}_{-0.9}$	102^{+79}_{-42}
GW231109 (QUR)	$2.30^{+0.44}_{-0.32}$	$13.3^{+0.8}_{-1.0}$	103^{+87}_{-41}
GW231109 $(a_i \le 0.4)$	$2.29^{+0.44}_{-0.32}$	$13.4^{+0.8}_{-1.1}$	103^{+77}_{-42}
$\mathrm{GW}231109~(\mathtt{XAS})$	$2.31^{+0.38}_{-0.34}$	$13.3^{+0.8}_{-1.3}$	103^{+75}_{-48}
GW170817	$2.19^{+0.38}_{-0.29}$	$12.2^{+1.1}_{-1.4}$	84^{+64}_{-47}
GW190425	$2.28^{+0.40}_{-0.31}$	$13.5^{+0.7}_{-0.9}$	104_{-39}^{+71}
GW170817+GW231109	$2.21^{+0.41}_{-0.33}$	$12.2^{+1.0}_{-1.2}$	82^{+72}_{-40}
GW170817+GW190425	$2.21_{-0.29}^{+0.35}$	$12.3_{-1.2}^{+1.2}$	84^{+60}_{-41}
GW170817+GW190425+GW231109	$2.22^{+0.34}_{-0.31}$	$12.1^{+1.1}_{-1.2}$	83 ⁺⁶⁴ ₋₃₉

- [15] G. Ghirlanda et al., Science 363, 968 (2019), arXiv:1808.00469 [astro-ph.HE].
- [16] E. Troja et al., Nature 551, 71 (2017), arXiv:1710.05433 [astro-ph.HE].
- [17] P. D'Avanzo et al., Astron. Astrophys. 613, L1 (2018), arXiv:1801.06164 [astro-ph.HE].
- [18] B. P. Abbott et al. (LIGO Scientific, Virgo, 1M2H, Dark Energy Camera GW-E, DES, DLT40, Las Cumbres Observatory, VINROUGE, MASTER), Nature 551, 85 (2017), arXiv:1710.05835 [astro-ph.CO].
- [19] B. P. Abbott et al. (LIGO Scientific, Virgo), Phys. Rev. Lett. 121, 161101 (2018), arXiv:1805.11581 [gr-qc].
- [20] B. P. Abbott *et al.* (LIGO Scientific, Virgo), Astrophys.
 J. Lett. 892, L3 (2020), arXiv:2001.01761 [astro-ph.HE].
- [21] R. J. Foley, D. A. Coulter, C. D. Kilpatrick, A. L. Piro, E. Ramirez-Ruiz, and J. Schwab, Mon. Not. Roy. Astron. Soc. 494, 190 (2020), arXiv:2002.00956 [astro-ph.HE].

- [22] M.-Z. Han, S.-P. Tang, Y.-M. Hu, Y.-J. Li, J.-L. Jiang, Z.-P. Jin, Y.-Z. Fan, and D.-M. Wei, Astrophys. J. Lett. 891, L5 (2020), arXiv:2001.07882 [astro-ph.HE].
- [23] K. Kyutoku, S. Fujibayashi, K. Hayashi, K. Kawaguchi, K. Kiuchi, M. Shibata, and M. Tanaka, Astrophys. J. Lett. 890, L4 (2020), arXiv:2001.04474 [astro-ph.HE].
- [24] R. Dudi, A. Adhikari, B. Brügmann, T. Dietrich, K. Hayashi, K. Kawaguchi, K. Kiuchi, K. Kyutoku, M. Shibata, and W. Tichy, Phys. Rev. D 106, 084039 (2022), arXiv:2109.04063 [astro-ph.HE].
- [25] J. C. Rastinejad et al., Nature 612, 223 (2022), arXiv:2204.10864 [astro-ph.HE].
- [26] E. Troja et al., Nature $\bf 612$, 228 (2022), arXiv:2209.03363 [astro-ph.HE].
- [27] N. Kunert et al., Mon. Not. Roy. Astron. Soc. 527, 3900 (2024), arXiv:2301.02049 [astro-ph.HE].
- [28] A. J. Levan et al. (JWST), Nature 626, 737 (2024), arXiv:2307.02098 [astro-ph.HE].

- [29] J. Aasi et al. (LIGO Scientific), Class. Quant. Grav. 32, 074001 (2015), arXiv:1411.4547 [gr-qc].
- [30] F. Acernese et al. (VIRGO), Class. Quant. Grav. 32, 024001 (2015), arXiv:1408.3978 [gr-qc].
- [31] A. G. Abac et al. (LIGO Scientific, VIRGO, KAGRA), (2025), arXiv:2508.18082 [gr-qc].
- [32] W. Niu et al., (2025), arXiv:2509.09741 [astro-ph.HE].
- [33] B. P. Abbott et al. (LIGO Scientific, Virgo), Phys. Rev. X 9, 011001 (2019), arXiv:1805.11579 [gr-qc].
- [34] Z. Li, Z. Chen, Y. Huang, Y. Lu, and J. Liu, (2025), arXiv:2509.14124 [astro-ph.HE].
- [35] M. Punturo et al., Class. Quant. Grav. 27, 194002 (2010).
- [36] S. Hild et al., Class. Quant. Grav. 28, 094013 (2011), arXiv:1012.0908 [gr-qc].
- [37] D. Reitze et al., Bull. Am. Astron. Soc. 51, 035 (2019), arXiv:1907.04833 [astro-ph.IM].
- [38] M. Evans et al., (2021), arXiv:2109.09882 [astro-ph.IM].
- [39] M. Evans et al., (2023), arXiv:2306.13745 [astro-ph.IM].
- [40] J. Skilling, AIP Conf. Proc. **735**, 395 (2004).
- [41] J. Skilling, Bayesian Analysis 1, 833 (2006).
- [42] J. S. Speagle, Mon. Not. Roy. Astron. Soc. 493, 3132 (2020), arXiv:1904.02180 [astro-ph.IM].
- [43] S. Koposov, J. Speagle, K. Barbary, G. Ashton, E. Bennett, J. Buchner, C. Scheffler, B. Cook, C. Talbot, J. Guillochon, P. Cubillos, A. A. Ramos, M. Dartiailh, Ilya, E. Tollerud, D. Lang, B. Johnson, jtmendel, E. Higson, T. Vandal, T. Daylan, R. Angus, patelR, P. Cargile, P. Sheehan, M. Pitkin, M. Kirk, J. Leja, joezuntz, and D. Goldstein, "joshspeagle/dynesty: v2.1.4," (2024).
- [44] G. Ashton et al., Astrophys. J. Suppl. 241, 27 (2019), arXiv:1811.02042 [astro-ph.IM].
- [45] A. Abac, T. Dietrich, A. Buonanno, J. Steinhoff, and M. Ujevic, Phys. Rev. D 109, 024062 (2024), arXiv:2311.07456 [gr-qc].
- [46] M. Colleoni, F. A. Ramis Vidal, N. K. Johnson-McDaniel, T. Dietrich, M. Haney, and G. Pratten, Phys. Rev. D 111, 064025 (2025), arXiv:2311.15978 [gr-qc].
- [47] T. Dietrich, T. Hinderer, and A. Samajdar, Gen. Rel. Grav. 53, 27 (2021), arXiv:2004.02527 [gr-qc].
- [48] K. Chatziioannou, Gen. Rel. Grav. 52, 109 (2020), arXiv:2006.03168 [gr-qc].
- [49] N. J. Cornish and T. B. Littenberg, Class. Quant. Grav. 32, 135012 (2015), arXiv:1410.3835 [gr-qc].
- [50] T. B. Littenberg and N. J. Cornish, Phys. Rev. D 91, 084034 (2015), arXiv:1410.3852 [gr-qc].
- [51] N. J. Cornish, T. B. Littenberg, B. Bécsy, K. Chatziioannou, J. A. Clark, S. Ghonge, and M. Millhouse, Phys. Rev. D 103, 044006 (2021), arXiv:2011.09494 [grqc].
- [52] A. G. Abac et al. (LIGO Scientific, VIRGO, KAGRA), (2025), arXiv:2508.18079 [gr-qc].
- [53] R. Abbott et al. (KAGRA, VIRGO, LIGO Scientific), Astrophys. J. Suppl. 267, 29 (2023), arXiv:2302.03676 [gr-qc].
- [54] R. Abbott et al. (LIGO Scientific, Virgo), SoftwareX 13, 100658 (2021), arXiv:1912.11716 [gr-qc].
- [55] C. García-Quirós, S. Husa, M. Mateu-Lucena, and A. Borchers, Class. Quant. Grav. 38, 015006 (2021), arXiv:2001.10897 [gr-qc].
- [56] S. Morisaki, Phys. Rev. D 104, 044062 (2021), arXiv:2104.07813 [gr-qc].

- [57] R. Smith, S. E. Field, K. Blackburn, C.-J. Haster,
 M. Pürrer, V. Raymond, and P. Schmidt, Phys. Rev.
 D 94, 044031 (2016), arXiv:1604.08253 [gr-qc].
- [58] S. Morisaki, R. Smith, L. Tsukada, S. Sachdev, S. Stevenson, C. Talbot, and A. Zimmerman, Phys. Rev. D 108, 123040 (2023), arXiv:2307.13380 [gr-qc].
- [59] I. M. Romero-Shaw et al., Mon. Not. Roy. Astron. Soc. 499, 3295 (2020), arXiv:2006.00714 [astro-ph.IM].
- [60] P. Landry and J. S. Read, Astrophys. J. Lett. 921, L25 (2021), arXiv:2107.04559 [astro-ph.HE].
- [61] R. Abbott et al. (KAGRA, VIRGO, LIGO Scientific), Phys. Rev. X 13, 011048 (2023), arXiv:2111.03634 [astro-ph.HE].
- [62] F. Ozel, D. Psaltis, R. Narayan, and A. S. Villarreal, Astrophys. J. 757, 55 (2012), arXiv:1201.1006 [astro-ph.HE].
- [63] B. Kiziltan, A. Kottas, M. De Yoreo, and S. E. Thorsett, Astrophys. J. 778, 66 (2013), arXiv:1309.6635 [astro-ph.SR].
- [64] F. Özel and P. Freire, Ann. Rev. Astron. Astrophys. 54, 401 (2016), arXiv:1603.02698 [astro-ph.HE].
- [65] J. Schwab, P. Podsiadlowski, and S. Rappaport, Astrophys. J. 719, 722 (2010), arXiv:1006.4584 [astroph.HE].
- [66] J. Antoniadis, T. M. Tauris, F. Ozel, E. Barr, D. J. Champion, and P. C. C. Freire, (2016), arXiv:1605.01665 [astro-ph.HE].
- [67] J. Alsing, H. O. Silva, and E. Berti, Mon. Not. Roy. Astron. Soc. 478, 1377 (2018), arXiv:1709.07889 [astro-ph.HE].
- [68] N. Farrow, X.-J. Zhu, and E. Thrane, Astrophys. J. 876, 18 (2019), arXiv:1902.03300 [astro-ph.HE].
- [69] D.-S. Shao, S.-P. Tang, J.-L. Jiang, and Y.-Z. Fan, Phys. Rev. D 102, 063006 (2020), arXiv:2009.04275 [astro-ph.HE].
- [70] J. E. Horvath, L. S. Rocha, A. L. C. Bernardo, M. G. B. de Avellar, and R. Valentim, (2020), arXiv:2011.08157 [astro-ph.HE].
- [71] J. W. T. Hessels, S. M. Ransom, I. H. Stairs, P. C. C. Freire, V. M. Kaspi, and F. Camilo, Science 311, 1901 (2006), arXiv:astro-ph/0601337.
- [72] T. Dietrich, N. Moldenhauer, N. K. Johnson-McDaniel, S. Bernuzzi, C. M. Markakis, B. Brügmann, and W. Tichy, Phys. Rev. D 92, 124007 (2015), arXiv:1507.07100 [gr-qc].
- [73] T. Hinderer, B. D. Lackey, R. N. Lang, and J. S. Read, Phys. Rev. D 81, 123016 (2010), arXiv:0911.3535 [astro-ph.HE].
- [74] T. Damour and A. Nagar, Phys. Rev. D 80, 084035 (2009), arXiv:0906.0096 [gr-qc].
- [75] T. Damour, A. Nagar, and L. Villain, Phys. Rev. D 85, 123007 (2012), arXiv:1203.4352 [gr-qc].
- [76] K. Yagi and N. Yunes, Class. Quant. Grav. 33, 13LT01 (2016), arXiv:1512.02639 [gr-qc].
- [77] K. Chatziioannou, C.-J. Haster, and A. Zimmerman, Phys. Rev. D 97, 104036 (2018), arXiv:1804.03221 [gr-qc].
- [78] W. Kastaun and F. Ohme, Phys. Rev. D 100, 103023 (2019), arXiv:1909.12718 [gr-qc].
- [79] H. Koehn et al., Phys. Rev. X 15, 021014 (2025), arXiv:2402.04172 [astro-ph.HE].
- [80] H. Rose, https://multi-messenger.physik.uni-potsdam.de/eos_constraints/ (2024), An

- overview of existing and new nuclear and astrophysical constraints on the equation of state of neutron-rich dense matter.
- [81] P. T. H. Pang et al., Nature Commun. 14, 8352 (2023), arXiv:2205.08513 [astro-ph.HE].
- [82] A. G. Abac et al. (LIGO Scientific, KAGRA, VIRGO), Astrophys. J. Lett. 970, L34 (2024), arXiv:2404.04248 [astro-ph.HE].
- [83] L. Santamaria et al., Phys. Rev. D 82, 064016 (2010), arXiv:1005.3306 [gr-qc].
- [84] P. Ajith et al., Phys. Rev. Lett. 106, 241101 (2011), arXiv:0909.2867 [gr-qc].
- [85] E. E. Flanagan and T. Hinderer, Phys. Rev. D 77, 021502 (2008), arXiv:0709.1915 [astro-ph].
- [86] M. Favata, Phys. Rev. Lett. 112, 101101 (2014), arXiv:1310.8288 [gr-qc].
- [87] K. K. Y. Ng, S. Vitale, A. Zimmerman, K. Chatziioannou, D. Gerosa, and C.-J. Haster, Phys. Rev. D 98, 083007 (2018), arXiv:1805.03046 [gr-qc].
- [88] J. Lin, IEEE Trans. Info. Theor. 37, 145 (1991).
- [89] T. Wouters, P. T. H. Pang, H. Koehn, H. Rose, R. Somasundaram, I. Tews, T. Dietrich, and C. Van Den Broeck, Phys. Rev. D 112, 043037 (2025), arXiv:2504.15893 [astro-ph.HE].
- [90] F. Douchin and P. Haensel, Astron. Astrophys. 380, 151 (2001), arXiv:astro-ph/0111092.
- [91] I. Tews, J. Margueron, and S. Reddy, Phys. Rev. C 98, 045804 (2018), arXiv:1804.02783 [nucl-th].
- [92] J. Margueron, R. Hoffmann Casali, and F. Gulminelli, Phys. Rev. C 97, 025805 (2018), arXiv:1708.06894 [nucl-th].
- [93] J. Margueron, R. Hoffmann Casali, and F. Gulminelli, Phys. Rev. C 97, 025806 (2018), arXiv:1708.06895 [nucl-th].
- [94] R. Somasundaram, C. Drischler, I. Tews, and J. Margueron, Phys. Rev. C 103, 045803 (2021), arXiv:2009.04737 [nucl-th].
- [95] S. K. Greif, G. Raaijmakers, K. Hebeler, A. Schwenk, and A. L. Watts, Mon. Not. Roy. Astron. Soc. 485, 5363 (2019), arXiv:1812.08188 [astro-ph.HE].
- [96] I. Tews, J. Margueron, and S. Reddy, Eur. Phys. J. A 55, 97 (2019), arXiv:1901.09874 [nucl-th].
- [97] R. Somasundaram, I. Tews, and J. Margueron, Phys. Rev. C 107, 025801 (2023), arXiv:2112.08157 [nucl-th].
- [98] R. Frostig, M. J. Johnson, and C. Leary, Systems for Machine Learning 4 (2018).
- [99] M. Gabrié, G. M. Rotskoff, and E. Vanden-Eijnden, Proc. Nat. Acad. Sci. 119, e2109420119 (2022), arXiv:2105.12603 [physics.data-an].
- [100] K. W. k. Wong, M. Gabrié, and D. Foreman-Mackey, J. Open Source Softw. 8, 5021 (2023), arXiv:2211.06397 [astro-ph.IM].
- [101] P. Demorest, T. Pennucci, S. Ransom, M. Roberts, and J. Hessels, Nature 467, 1081 (2010), arXiv:1010.5788 [astro-ph.HE].
- [102] M. Shamohammadi et al., Mon. Not. Roy. Astron. Soc. 520, 1789 (2023), arXiv:2212.04051 [astro-ph.HE].
- [103] E. Fonseca et al., Astrophys. J. Lett. 915, L12 (2021), arXiv:2104.00880 [astro-ph.HE].
- [104] H. T. Cromartie et al. (NANOGrav), Nature Astron. 4, 72 (2019), arXiv:1904.06759 [astro-ph.HE].
- [105] T. E. Riley et al., Astrophys. J. Lett. 918, L27 (2021), arXiv:2105.06980 [astro-ph.HE].

- [106] T. Salmi et al., Astrophys. J. 941, 150 (2022), arXiv:2209.12840 [astro-ph.HE].
- [107] M. C. Miller et al., Astrophys. J. Lett. 918, L28 (2021), arXiv:2105.06979 [astro-ph.HE].
- [108] G. Agazie et al. (NANOGrav), Astrophys. J. Lett. 951, L9 (2023), arXiv:2306.16217 [astro-ph.HE].
- [109] A. J. Dittmann et al., Astrophys. J. 974, 295 (2024), arXiv:2406.14467 [astro-ph.HE].
- [110] T. Salmi et al., Astrophys. J. 974, 294 (2024), arXiv:2406.14466 [astro-ph.HE].
- [111] N. D. Cao, I. Titov, and W. Aziz, "Block neural autoregressive flow," (2019), arXiv:1904.04676 [stat.ML].
- [112] D. Ward, "FLOWJAX: Distributions and normalizing flows in JAX," (2024).
- [113] A. Ray, M. Camilo, J. Creighton, S. Ghosh, and S. Morisaki, Phys. Rev. D 107, 043035 (2023), arXiv:2211.06435 [gr-qc].
- [114] W. Del Pozzo, T. G. F. Li, M. Agathos, C. Van Den Broeck, and S. Vitale, Phys. Rev. Lett. 111, 071101 (2013), arXiv:1307.8338 [gr-qc].
- [115] B. D. Lackey and L. Wade, Phys. Rev. D 91, 043002 (2015), arXiv:1410.8866 [gr-qc].
- [116] F. Hernandez Vivanco, R. Smith, E. Thrane, P. D. Lasky, C. Talbot, and V. Raymond, Phys. Rev. D 100, 103009 (2019), arXiv:1909.02698 [gr-qc].
- [117] K. Hotokezaka, K. Kyutoku, H. Okawa, M. Shibata, and K. Kiuchi, Phys. Rev. D 83, 124008 (2011), arXiv:1105.4370 [astro-ph.HE].
- [118] K. Hotokezaka, K. Kiuchi, K. Kyutoku, T. Muranushi, Y.-i. Sekiguchi, M. Shibata, and K. Taniguchi, Phys. Rev. D 88, 044026 (2013), arXiv:1307.5888 [astro-ph.HE].
- [119] N. Sarin and P. D. Lasky, Gen. Rel. Grav. 53, 59 (2021), arXiv:2012.08172 [astro-ph.HE].
- [120] S. Bernuzzi, Gen. Rel. Grav. 52, 108 (2020), arXiv:2004.06419 [astro-ph.HE].
- [121] A. Puecher and T. Dietrich, Phys. Rev. D 110, 123038 (2024), arXiv:2408.10678 [astro-ph.HE].
- [122] J. H. Friedman, Annals of statistics , 1189 (2001).
- [123] J. H. Friedman, Computational Statistics & Data Analysis 38, 367 (2002), nonlinear Methods and Data Mining.
- [124] T. Dietrich, M. W. Coughlin, P. T. H. Pang, M. Bulla, J. Heinzel, L. Issa, I. Tews, and S. Antier, Science 370, 1450 (2020), arXiv:2002.11355 [astro-ph.HE].
- [125] M. Bulla, Mon. Not. Roy. Astron. Soc. 489, 5037 (2019), arXiv:1906.04205 [astro-ph.HE].
- [126] M. Bulla, Mon. Not. Roy. Astron. Soc. 520, 2558 (2023), arXiv:2211.14348 [astro-ph.HE].
- [127] S. Fujibayashi, K. Kiuchi, N. Nishimura, Y. Sekiguchi, and M. Shibata, Astrophys. J. 860, 64 (2018), arXiv:1711.02093 [astro-ph.HE].
- [128] K. A. Lund, R. Somasundaram, G. C. McLaughlin, J. M. Miller, M. R. Mumpower, and I. Tews, (2024), arXiv:2408.07686 [astro-ph.HE].
- [129] M. M. Kasliwal et al., Astrophys. J. 905, 145 (2020), arXiv:2006.11306 [astro-ph.HE].
- [130] T. Ahumada et al., Publ. Astron. Soc. Pac. 136, 114201 (2024), arXiv:2405.12403 [astro-ph.HE].
- [131] F. B. Bianco et al., Astrophys. J. Supp. 258, 1 (2022), arXiv:2108.01683 [astro-ph.IM].
- [132] M. Maggiore et al. (ET), JCAP 03, 050 (2020), arXiv:1912.02622 [astro-ph.CO].
- [133] A. Abac et al., (2025), arXiv:2503.12263 [gr-qc].

- [134] S. Danilishin and T. Zhang, Einstein Telescope sensitivity curves used for CoBA Science study, Tech. Rep. ET-0304A-22 (Einstein Telescope Collaboration, 2022).
- [135] Cosmic Explorer Strain Sensitivity, Tech. Rep. CE-T2000017-v8 (Cosmic Explorer Project, 2020).
- [136] R. Gamba, M. Breschi, S. Bernuzzi, M. Agathos, and A. Nagar, Phys. Rev. D 103, 124015 (2021),
- $arXiv{:}2009.08467~[gr\mbox{-}qc].$
- [137] G. Pratten, P. Schmidt, and N. Williams, Phys. Rev. Lett. 129, 081102 (2022), arXiv:2109.07566 [astro-ph.HE].
- [138] N. Kunert, P. T. H. Pang, I. Tews, M. W. Coughlin, and T. Dietrich, Phys. Rev. D 105, L061301 (2022), arXiv:2110.11835 [astro-ph.HE].